Journal of Energy Storage 31 (2020) 101701

Contents lists available at ScienceDirect

Journal of Energy Storage

journal homepage: www.elsevier.com/locate/est

Transient phase change heat transfer in a metal foam-phase change material heatsink subject to a pulse heat flux

Ahmad Hajjar[a], Esmail Jamesahar[b], Hassan Shirivand[c], Mohammad Ghalambaz[d,e], Roohollah Babaei Mahani[f,g,*]

[a] ECAM Lyon, LabECAM, Université de Lyon, Lyon, France
[b] Young Researchers and Elite Club, Ahvaz Branch, Islamic Azad University, Ahvaz, Iran
[c] Faculty of Mechanical and Energy Engineering, Shahid Beheshti University, Tehran, Iran
[d] Metamaterials for Mechanical, Biomechanical and Multiphysical Applications Research Group, Ton Duc Thang University, Ho Chi Minh City, Vietnam
[e] Faculty of Applied Sciences, Ton Duc Thang University, Ho Chi Minh City, Vietnam
[f] Institute of Research and Development, Duy Tan University, Da Nang, 550000, Vietnam
[g] Faculty of Civil Engineering, Duy Tan University, Da Nang, 550000, Vietnam

ARTICLE INFO

Keywords:
Metal foam composite
Phase change materials
Phase change heatsink
Pulse heat flux

ABSTRACT

In the present study, the effect of using a layer of metal foam in a composite metal foam – phase change heatsink is addressed. The bottom of the heatsink is subjected to a pulse heat flux, while the top of the heatsink is exposed to an external cooling convective flow. The melting/solidification of the Phase Change Materials (PCMs) is modeled using the enthalpy porosity approach. The partial differential equations governing the natural convective flow and the heat transfer in the clear flow region and porous layers of the heatsink are introduced and transformed into a non-dimensional form using non-dimensional variables. The Finite Element Method (FEM) with an automatic time-step and grid adaptation is employed to solve the governing equations. The model and the numerical code are validated by comparison to several results obtained in recent works available in the literature. The effect of the surrounding heat transfer by convection and the fusion temperature of the PCM on the heatsink performance and on the phase change behavior is investigated. The results show that melting heat transfer occurs during the activation of the pulse heat flux while the solidification commences with a small delay after the pulse heat flux turns off. The heatsink presents a major benefit when the external cooling power is weak. Moreover, a heatsink with a lower fusion temperature shows a better cooling efficiency. The presence of a metal foam layer notably improves the cooling efficiency of the heatsink. However, the location of the porous layer shows a minimal effect on the heatsink efficiency.

1. Introduction

Phase Change Materials (PCMs) can store/release a significant amount of energy on phase change [1]. Due to the high density of latent heat, a notable amount of heat could be stored in a small amount of mass. Thus, PCMs are potential means for various thermal energy storage and thermal management systems in applications such as peak load shifting [2], reducing the size of thermal systems, and damping of transient heat loads. PCMs have found promising applications in energy storage for solar processes [3], solar domestic water heating systems [4], various parts of building [5], thermal management of photovoltaic power systems [6], automotive industry [7], general thermal energy storage [8,9], and thermal management of electronic components [10].

Typically, industrial and commercial electronic components are designed to be operated below 100°C. However, the electronic components produce a significant amount of waste heat during their operation, depending on their loading conditions. Hence, they demand a proper cooling mechanism to keep them within their design temperature [10]. In many applications, including computer processors, radars and weapon systems, the produced waste heat of an electronic component is transient with a notable peak-load. Designing a thermal system for the highest peak load leads to an oversized cooling system, which is extremely undesired. As the thermal peak-load is a transient situation, the cooling system can be designed for average heat load through an energy storage system as a buffer to damp the peak loads. Although PCMs are capable of storing/releasing a significant amount of

* Corresponding author.
E-mail addresses: ahmad.hajjar@ecam.fr (A. Hajjar), mohammad.ghalambaz@tdtu.edu.vn (M. Ghalambaz), roohollahbabaeimahani@duytan.edu.vn (R. Babaei Mahani).

https://doi.org/10.1016/j.est.2020.101701
Received 9 January 2020; Received in revised form 25 May 2020; Accepted 18 July 2020
Available online 05 August 2020

Nomenclature

Latin symbols

A_{mush}	a big value in the order $O(10^5)$
Bi	Biot number, defined as $h_\infty H/k_{m,l}$
C_p	specific heat capacity ($J.kg^{-1}.K^{-1}$)
dA	the differential surface area of the heatsink (m^2)
Da	Darcy number, defined as κ/H^2
e	small number in the order $O(10^{-3})$
g	constant of gravity ($m.s^{-2}$)
h	coefficient of thermal convection ($W.m^{-2}.K^{-1}$)
H	characteristic length (l_h) (m)
h_{sf}	fusion latent heat ($J.kg^{-1}$)
k	number of elements, thermal conductivity ($W.m^{-1}.K^{-1}$),
l_h	height of the heatsink (m)
L_h	dimensionless height of the heatsink
l_{hp}	height of the porous foam (m)
L_{hp}	dimensionless height of the porous foam
l_w	width of the heatsink (m)
L_w	dimensionless width of the heatsink
l_{wp}	width of the porous foam (m)
L_{wp}	dimensionless width of the porous foam
MVF	the molten portion of the heatsink
n	normal to a surface (m)
N	dimensionless normal to a surface, total number of elements
p	pressure (Pa)
P	dimensionless pressure
Pr	Prandtl number, $\nu/\alpha_{m,l}$
q''	heat flux ($W.m^2$)
q_0''	element heat flux ($W.m^{-2}$)
R	residual equation
Ra	Rayleigh number, $(g\beta_l\Delta TH^3)/(\nu_l\alpha_{m,l})$
s	phase change source term in the momentum equation
S	dimensionless source term in the dimensionless momentum equation
Ste	Stefan number, $((\rho C_p)_{m,l}\,\Delta T)/(\rho_l h_{sf})$
s_w, s_b, s_t	the thicknesses of the conjugate walls defined in Fig. 1 (m)
S_w, S_b, S_t	dimensionless the thicknesses of the conjugate walls
t	time (s)
T	temperature (K)
u	x-component of the velocity ($m.s^{-1}$)
U	dimensionless x-component of the velocity
v	y-component of the velocity ($m.s^{-1}$)
V	dimensionless y-component of the velocity
X	dimensionless x-coordinate, x/H
x	x-coordinate (m)
X	dimensionless X-coordinate
y	y-coordinate (m)
Y	dimensionless Y-coordinate

Greek symbols

α	thermal diffusivity ($m^2.s^{-1}$)
β	coefficient of volume expansion (K^{-1})
γ	basis function for FEM
δ	dimensionless heat flux
δt	duration of the heat pulse (s)
δT	fusion temperature band (K)
ΔT	reference temperature scale (K), defined as $q''_0 H/k_{m,l}$
$\Delta\tau$	dimensionless duration of the heat pulse
ε	metal foam porosity
η	heatsink efficiency
θ	dimensionless temperature $(T\text{-}T_\infty)/\Delta T$
κ	metal foam permeability (m^2)
μ	dynamic viscosity ($kg.m^{-1}.s^{-1}$)
ν	kinematic viscosity ($kg.m^{-1}.s^{-1}$)
ρ	density ($kg.m^{-3}$)
τ	non-dimensional time
ϕ	volume fraction of the melted PCM

Subscripts

0	initial steady-state solution
1	start of heat pulse
2	end of heat pulse
∞	external cooling flow
ave	average
b	hot surface
f	fusion
i	dummy variable of the numerical scheme
l	liquid/molten PCM
m	effective of the PCM and porous matrix, dummy variable of the numerical scheme
s	solid PCM
w	wall, copper shell

latent thermal energy, their low thermal conductivity is a barrier to their applications in many thermal management systems, particularly when a notable amount of energy shall be stored or released in a short time. Thus, the current research focuses on the engagement of the heat transfer capability of PCM, by employing nano-additives [11,12], micro-encapsulation techniques [13,14], metal inserters (fins) [15], and metal foams [16,17].

Phase change melting/solidification of PCM embedded in metal foams has been subject of some of the recent researches for electronic applications due to the essential advantages metal foams such as lightweight, high thermal enhancement, and good mechanical properties. The latent heat of PCMs contributes to the thermal energy storage of the electronic component, while the metal foam contributes to heat transfer enhancement. Hence, the peak heat loads of an electronic component can be stored in the PCM heatsink quickly and uniformly.

Considering metal foams and phase change materials, Xiao et al. [18] synthesized samples of paraffin wax embedded in copper and nickel metal foam. They prepared samples of metal foams with porosities in the range of 92.5 to 97.5%. The measurements of the effective thermal conductivity of the metal foam and paraffin wax demonstrate a significant enhancement of thermal conductivity. The thermal conductivities of the paraffin/nickel foam composite and paraffin/copper foam composite PCMs are three folds and 15 folds better than the that of pure paraffin, respectively. A slight shift of fusion temperature for paraffin, embedded in a porous matrix, was observed. Zheng et al. [19] investigated the melting heat transfer of paraffin wax in a square cavity enclosure. They reported the phase change behavior in the presence or absence of a copper foam porous matrix. It was found that the presence of copper metal foam improves the melting heat transfer. However, the natural convection heat transfer in the porous space is also notable and cannot be neglected. The PCMs are usually enclosed in containers to avoid leakage and mechanical problems. The geometry and structure of the enclosure can be changed notably, depending on the application and design of thermal management or energy storage systems. An excellent review of the shape of PCMs enclosures is performed by Dinker et al. [20]. They found that the low thermal conductivity of both inorganic and organic PCMs has restricted their direct commercial-scale applications. Compositing PCMs with high thermal conductivity

materials such as metallic nanoparticles, metal oxides, carbon nanotubes, and graphite can improve the thermal conductivity of PCMs. The authors reported that different geometrical configurations such as rectangular shell and tube, cylindrical shell and tube and triplex and configurations with axial and longitudinal fins have been used as containers of PCMs. Although, the presence of fins shortens the energy storage time of the phase change materials, it declines the total space of the container, and consequently, the weight of phase change materials reduces. As a result, the presence of the metal fins improves the melting response time but reduces the overall capacity of energy storage.

The natural convection has a positive effect on the melting heat transfer of PCMs, which improves the heat transfer and declines the melting time. Various aspects of natural convection in enclosures have been addressed, such as metal foams [21], phase change composites [22], cavity partially filled with a porous medium [23], conjugate heat transfer [24,25], nano-additives [26–28], magneto-hydrodynamic effects [29, 30], and entropy generation [31]. In the case of using nano-additives, the stability in the molten state is a concern as settling of the fillers will change the effective thermal conductivity. This is a reason to pursue foams over nano additives [22]. The presence of a porous medium with high thermal conductivity in an enclosure improves the conduction heat transfer but suppresses the natural convection heat transfer. The presence of nano-additives improves the theral conductivity of the liquid, but they weaken the natural convection flows by elevating the dynamic viscosity and declining the buoyancy effects. Using highly conductive porous composite made of carbon nanotubes, the magnetic forces also tend to suppress the natural convection flows by resisting the fluid motion.

Regarding the phase change heat transfer in enclosure heatsinks, Bondareva et al. investigated the phase change behavior of n-Octadecane enhanced with alumina nanoparticles in a horizontal [32] and an inclined heatsink [12]. The outcomes show that using nanoparticles increases the viscosity of liquid PCM and deteriorates the heat transfer by convection, in convective dominant heat transfer regimes, particularly for small inclination angles. The effects of a hot heat generative element [33] and a local heat source [34] are also investigated.

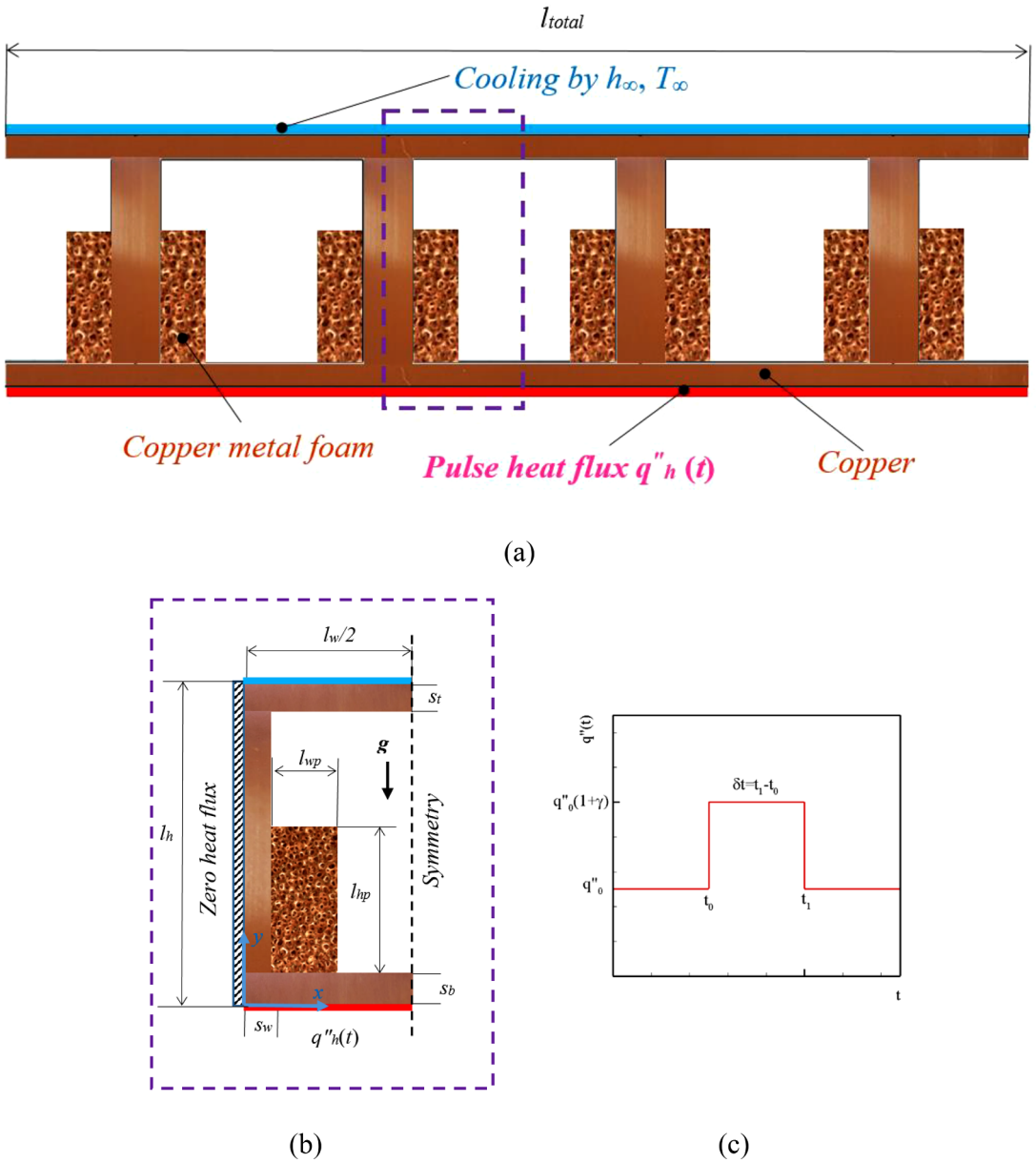

Fig. 1. Schematic view of the model; (a): overall view of PCM-Metal foam heatsink; (b): detailed view of one block of PCM-Metal foam heatsink with geometrical details; (c): the heat flux profile

Ghalambaz et al. [35,36] utilized nano-encapsulated phase change materials to improve the natural convection heat transfer. The results show that the encapsulation of PCMs is a promising approach to improve the phase change response and heat transfer. A composite capsulation [37] is also a promising approach to improve the thermal conductivity and phase change response of PCMs.

Hossain et al. [38] investigated the melting phase change in a cavity enclosure filled with a porous medium. It was found that the presence of a porous medium accelerates the movement of melting interfaces. Hussain et al. [39] used paraffin as the PCM and nickel as metal foam for thermal management of a pack of 3.4 Ah capacities 18650 Li-ion battery cells during the thermal loads of charging and discharging. The experimental results show that using nickel foam-paraffin composite reduces the surface temperature of the battery, about 31% compared to a case of cooling by air. Using nickel foam-paraffin reduces the temperature surface of the battery, about 24%, as compared to pure paraffin. Dinesh et al. [37] explored the effect of pore geometry of metal foams on the phase-change behavior of PCMs. The results show that the influence of overall porosity and overlap depends on the duration of energy absorption. Lower pore overlap and porosity are preferable for short heating times.

Wu et al. [40] utilized a composite of copper-mesh and paraffin and nano-additives for thermal management of a battery pack. The results reveal that the copper mesh is useful for producing a uniform cooling temperature for battery, particularly in harsh conditions. Zhu et al. [41] experimentally tested the effect using a layer of metal foam as a phase-change heat transfer enhancer in a composite PCM-metal foam heatsink. The heatsink was heated from below and partially filled with a layer of copper metal foam. The results demonstrate that 2/3 partial metal foam filling of the heatsink can provide a cooling performance about that of full filling. Hence, using a heatsink with a partial layer of metal foam reduces the cost and weight of the heatsink. Ghalambaz and Zhang [42] addressed the conjugate phase change heat transfer of PCMs in a cylindrical metal foam heatsink. The effect of the shell thickness of the heatsink was taken into account as a conjugate effect. The heatsink was filled with Nickle foam, and the shell was made of copper. The melting and solidification processes are investigated. The outcomes show that the melting heat transfer is much stronger than the solidification heat transfer due to the natural convection effects in liquid PCM. In the work of Ghalambaz and Zhang [42] the enclosure was an annulus fully filled with Nickle foam metal foam, and the was no fin involved to improve the heat transfer.

Although many electrical components are subject to a transient thermal load, there are only a few studies, which investigated the effect of transient thermal loads on the phase change behavior of a PCM heatsink. Moreover, using a partial layer of metal foam in the heatsink can reduce the production costs and weights of the PCM-heatsink. Following Ghalambaz and Zhang [42], the present work aims to theoretically address the effect of a partial layer of copper metal foam and its location on the phase-change heat transfer performance of a PCM-heatsink subject to a thermal pulse heat-flux for the first time. A pulse heat load consists of simultaneous melting and solidification processes, which involve the charging and discharging response of a metal foam heatsink.

2. Mathematical model

The heatsink investigated here is depicted in Fig. 1 (a). It is made of copper and is partially occupied by copper foam. PCM Paraffin wax is filling the porous space and the enclosure of the heatsink. The porosity and the permeability of the copper foam are denoted respectively by ε and κ, while the fusion temperature of the PCM is denoted by T_f. A pulse heat flux is applied at the heatsink bottom. The pulse heat flux has a base power q''_0, which increases to reach the power $(1 + \gamma)\, q''_0$ during a time interval δt, then returns to the value q''_0 for a longer period. The heatsink top is cooled by a convective heat transfer with a fluid of uniform temperature T_∞ and coefficient of convection h_∞, such that $T_\infty < T_f$. The PCM is initially at the temperature T_∞. The heatsink is then in steady-state, and the pulse heat flux remains at the base power q''_0 for a sufficiently long period. The heat flux rises suddenly at the instant t_0 to the high power value of $(1 + \gamma)\, q''_0$ during a time interval $\delta t = t_1 – t_0$, and gets back to the base power q''_0 at t_1. Fig. 1 (c) shows the profile of the heat flux at the bottom of the heatsink with respect to time. The metal foam, fins, PCM and boundary conditions for each cell of the heatsink are the same. An individual cell of the heatsink is indicated by the purple dashed line in Fig. 1 (a). This cell is depicted in Fig. 1 (b) in more details. Due to the similar behavior of the cells, only one cell is modeled here. Then, the results are converted to the unit length of the heatsink. Inside the enclosure, there is a coarse mesh with miniature thickness, which constrains the movement of solid bulks without interfering with the natural convection flow and heat transfer. The presence of a coarse woven mesh in heat pipes and phase change systems is common to limit the solid bulk movement for applications in vehicles and moveable machines in dynamic environments. In the present study, the contact thermal resistance between the copper fins and copper metal foam was neglected. This thermal resistance between two solid surfaces could play an essential role in the cooling of electronic devices. The thermal resistance depends on the type of thermal interface material between the metal foam and the surface upon which the heat flux is applied. In the present study, the enclosure is filled with PCM, and the empty pore spaces between the metal foam and the copper fins are in contact with the convective flow of the liquid PCM. Hence, the effect of the surface thermal resistance could be suppressed notably at the metal foam and fin side. In the present work, it is assumed that the copper foam and copper fin are e in good thermal contact, and hence, the effect of thermal resistance was neglected.

2.1. Governing equations

Considering the assumptions mentioned above, the equations governing the flow of molten paraffin wax and the heat transfer in the free layer and in the porous medium layer can be written as follows [43–45]:

$$\frac{\partial u}{\partial x} + \frac{\partial v}{\partial y} = 0 \tag{1}$$

$$\frac{\rho_l}{\varepsilon}\frac{\partial u}{\partial t} + \frac{\rho_l}{\varepsilon^2}\left(u\frac{\partial u}{\partial x} + v\frac{\partial u}{\partial y}\right) = -\frac{\partial p}{\partial x} + \frac{\mu_l}{\varepsilon}\left(\frac{\partial^2 u}{\partial x^2} + \frac{\partial^2 u}{\partial y^2}\right) - \frac{\mu_l}{\kappa}u - s(T)u \tag{2}$$

$$\frac{\rho_l}{\varepsilon}\frac{\partial v}{\partial t} + \frac{\rho_l}{\varepsilon^2}\left(u\frac{\partial v}{\partial x} + v\frac{\partial v}{\partial y}\right) = -\frac{\partial p}{\partial y} + \frac{\mu_l}{\varepsilon}\left(\frac{\partial^2 v}{\partial x^2} + \frac{\partial^2 v}{\partial y^2}\right) - \frac{\mu_l}{\kappa}v - s(T)v + \rho_l g\beta_l(T - T_f) \tag{3}$$

The energy balance in the metal foam is expressed by the following equation:

$$(\rho C_p)_m\frac{\partial T}{\partial t} + (\rho C_p)_l\left(u\frac{\partial T}{\partial x} + v\frac{\partial T}{\partial y}\right) = k_m\left(\frac{\partial^2 T}{\partial x^2} + \frac{\partial^2 T}{\partial y^2}\right) - \rho_l\varepsilon h_{sf}\frac{\partial \phi(T)}{\partial t} \tag{4}$$

where $(\rho C_p)_m = \phi(\rho C_p)_{m,l} + (1 - \phi)(\rho C_p)_{m,s}$, $(\rho c)_{m,l} = (1 - \varepsilon)(\rho C_p)_p + \varepsilon(\rho C_p)_l$and $(\rho c)_{m,s} = (1 - \varepsilon)(\rho C_p)_p + \varepsilon(\rho C_p)_s$. In Eqs. 1-4, the subscripts *l*, *s*, *p*, and *m* represent respectively the PCM liquid phase, PCM solid phase, the porous matrix, and the effective properties. The symbols ρ, μ, k, C_p, and h_{sf} denote the density, dynamic viscosity, thermal conductivity, heat capacity, and fusion latent heat, respectively.

The effective thermal conductivity of the PCM and the porous matrix is evaluated using the experimental data reported in [18] for a porous metal foam/paraffin-wax with the bulk porosity of $\varepsilon = 0.975$ and pores of 5 PPI. The permeability of the porous medium is also

selected based on the study of Bhattacharya et al. [46] as $\kappa = 2.7 \times 10^{-7}$ m^2. The effective thermal conductivity of the paraffin-wax and copper metal foam is considered as $k_m = 4.8$ W/m.K based on the measurements of Xiao et al. [18]. Table 1 reports the thermo-physical properties of copper metal foam and the paraffin phase change material.

In the momentum equations (2) and (3), a source term *s(T)* is introduced as

$$s(T) = A_{mush}\frac{(1-\phi(T))^2}{\phi(T)^3 + e} \tag{5}$$

with A_{mush} being a high number in the order $O(10^5)$ and e a tiny number in the order $O(10^{-3})$ to avoid having a zero denominator. *s(T)* represents a Darcy term in the porous medium, as it significantly increases to a very high value in the solid region to keep the velocity at zero, and nullifies in the liquid region.

The term $\phi(T)$ represents the volume fraction of the molten PCM. The phase change is assumed to occur when the temperature is close to the fusion temperature T_f, i.e. when the temperature is in a small range δT around T_f. Outside this range, the PCM is either totally solid ($\phi(T) = 0$), or totally liquid ($\phi(T) = 1$). Assuming that the volume fraction varies linearly as a function of temperature, $\phi(T)$ can be thus expressed as

$$\phi(T) = \begin{cases} 0 & T < T_f - \frac{\delta T}{2} \\ \frac{T - T_f}{\delta T} & T_f - \frac{\delta T}{2} < T < T_f + \frac{\delta T}{2} \\ 1 & T > T_f + \frac{\delta T}{2} \end{cases} \tag{6}$$

The PCM heat storage and release is controlled in the energy balance equation by the term $\frac{\partial \phi}{\partial t}$. This term is multiplied by the porosity, indicating that only the PCM in the pores is undergoing a phase change, while the porous matrix is not subject to any phase change. In addition, the viscosity is assumed to be a function of ϕ following the relation $\mu_l(\phi) = \mu_l + (1 - \phi)$. The viscosity in the liquid region is thus equal to the regular value μ_l, while in the solid region it rises to the maximum value $\mu_l + 1$, forcing the velocity components in the momentum equations to be zero. This assumption further contributes to a better stability of the solution and its convergence. The permeability of the metal foam is κ_0 and its porosity is ε_0. Therefore, $\kappa = \kappa_0$ and $\varepsilon(x, y) = \varepsilon_0$ in metal foam domain (Fig. 1 (a)). Otherwise, $\kappa \to \infty$ and $\varepsilon(x, y) = 1$ in the region with no metal foam.

It should be noted that the density of the solid paraffin is higher than the density of the liquid paraffin. Hence, it is not possible to have bulk solid paraffin floating in the liquid in a clear region with no constraint. Due to gravity effects and upward inadequate buoyancy forces, the solid bulk will sink and place at the bottom of the enclosure. However, in the present study, the phase change at the bottom takes place in the porous medium, which constraints the movability of the solid bulks of PCMs in the liquid and prevents them from sinking. Besides, the clear parts of the cavity are supported with a miniature mesh, which constrains the movement of solid bulk. Since the density variation during the phase change is neglected in the modeling approach, the motion of the solid bulks due to the gravity effects is automatically neglected and no modeling constraint is required to fix the bulk solid parts. Moreover, it is worth mentioning that the thermal buoyancy forces are modeled using the Boussinesq approximation, in which the densities are constant in all of the liquid domain except the thermal buoyancy force on the liquid region.

A no-slip boundary condition is set for the fluid flow on the walls. The walls are also impermeable. The following equation can be stated for the solid impermeable wall:

$$(\rho C_p)_w \frac{\partial T_w}{\partial t} = k_w\left(\frac{\partial^2 T_w}{\partial x^2} + \frac{\partial^2 T_w}{\partial y^2}\right) \tag{7}$$

A zero-pressure condition is set at the copper foam bottom left corner to serve as a reference pressure point. The sidewalls of the enclosure, due to the symmetry of the model, are adiabatic, such that

$$\frac{\partial T_w}{\partial n} = 0 \tag{8a}$$

where n is normal to the insulated walls. The equation governing the convective heat transfer at the top wall is written as:

$$k_w\frac{\partial T_w(x, l_h)}{\partial y} = h_\infty(T - T_\infty) \tag{8b}$$

The uniform heat flux at the bottom wall is expressed as:

$$k_w\frac{\partial T_w(x, 0)}{\partial y} = q''(t) \tag{8c}$$

where $q''(t) = \begin{cases} (1+\gamma)q & 0 < t < t_1 \\ q & t < 0,\ t > t_1 \end{cases}$.

The internal walls at the interface of the porous medium and solid walls are subject to temperature and heat flux continuity such that [47,48]:

$$T_w|_{wall} = T|_{porous} \quad and \quad k_w\left.\frac{\partial T_w}{\partial n}\right|_{wall} = k_m\left.\frac{\partial T}{\partial n}\right|_{porous} \tag{8d}$$

where n is the normal vector of the surface. The steady-state heatsink flow and temperature in the case of low power of the element heat flux, $q''(t) = q$ is adopted as the initial condition.

$$T(x, y, 0) = T@\text{ steady} - \text{state},\ u(x, y, 0) = u@\text{steady} - \text{state, and } v(x, y, 0) = v@\text{steady} - \text{state} \tag{8e}$$

In the above equations, it is assumed that the phase change density variations are small for paraffin wax, and hence, the volume changes due to the phase change are negligible. It is also assumed that there is a small void space in the third dimension to allow some degree of volume changes and diminish the surface stresses. These assumptions are in agreement with the experimental study of Zheng et al. [19], who experimentally and theistically investigated the melting of paraffin PCM in a copper metal foam. Validation with the experimental results of Zheng et al. [19] is also performed and reported in the validation section of the present study.

In order to write Equations (1)–(8) in the dimensionless form, the following non-dimensional variables are introduced:

$$X = \frac{x}{H},\ Y = \frac{y}{H},\ U = \frac{uH}{\alpha_{m,l}},\ V = \frac{vH}{\alpha_{m,l}},\ \theta = \frac{T - T_\infty}{\Delta T},\ \tau = \frac{t\alpha_{m,l}}{H^2},\ S(\theta) = \frac{s(T)H^2}{\rho_l\alpha_{m,l}}$$
$$P = \frac{pH^2}{\rho\alpha_{m,l}{}^2},\ \alpha_{m,l} = \frac{k_{m,l}}{(\rho c_p)_{m,l}},\ \Pr = \frac{\nu}{\alpha_{m,l}},\ Ra = \frac{g\beta_l\Delta T H^3}{\nu_l\alpha_{m,l}},\ Ste = \frac{(\rho Cp)_{m,l}\Delta T}{\rho_l h_{sf}} \tag{9}$$

where H is the characteristic length and is equal to l_h, Ra is the Rayleigh number, and Pr is the Prandtl number. The temperature is scaled using the characteristic value $\Delta T = q''H/k_{m,l}$ where $k_{m,l}$ represents the liquid PCM effective thermal conductivity.

Replacing the terms of Eq.(9) in Eqs. (1)–(8), the new Eqs. (10)–(20) are written in the dimensionless form as

Momentum in x-direction:

Table 1
The thermos-physical properties of paraffin wax PCM and copper metal foam [19]

Material	ρ (kg/m^3)	c_p (J/kg.K)	k (W/m.K)	h_{sf} (J/kg.K)	β (1/K)	μ (Pa.s)
Paraffin wax	900	2300	0.3	148800	0.0005	0.00324
Copper foam	8900	386	380	-	-	-

$$\frac{1}{\varepsilon}\frac{\partial U}{\partial \tau}+\frac{1}{\varepsilon^2}\left(U\frac{\partial U}{\partial X}+V\frac{\partial U}{\partial Y}\right)=-\frac{\partial P}{\partial X}+\eta(\phi)\frac{\Pr}{\varepsilon}\left(\frac{\partial^2 U}{\partial X^2}+\frac{\partial^2 U}{\partial Y^2}\right)-\eta(\phi)\frac{\Pr}{Da}U-S(\theta)U \tag{10}$$

Momentum in y-direction:

$$\frac{1}{\varepsilon}\frac{\partial V}{\partial \tau}+\frac{1}{\varepsilon^2}\left(U\frac{\partial V}{\partial X}+V\frac{\partial V}{\partial Y}\right)=-\frac{\partial P}{\partial Y}+\eta(\phi)\frac{\Pr}{\varepsilon}\left(\frac{\partial^2 V}{\partial X^2}+\frac{\partial^2 V}{\partial Y^2}\right)-\eta(\phi)\frac{\Pr}{Da}V-S(\theta)V+\Pr Ra\theta \tag{11}$$

The following geometrical dimensionless parameters are introduced: $S_w=s_w/H$, $S_b=s_b/H$, $S_t=s_t/H$, $L_h=l_h/H$, $L_{hp}=l_{hp}/H$, and $L_{wp}=l_{wp}/H$. In the above equations, the term $\eta(\phi)=1+(1-\phi)/(\rho_l\alpha_{m,l})$ artificially augments the viscosity to a large value in the solid domain, and helps the convergence of the solver.

The energy balance for melted PCM:

$$\frac{(\rho C_p)_m}{(\rho C_p)_{m,l}}\left(\frac{\partial\theta}{\partial\tau}\right)+\frac{(\rho C_p)_l}{(\rho C_p)_{m,l}}\left(U\frac{\partial\theta}{\partial X}+V\frac{\partial\theta}{\partial Y}\right)=\frac{k_m}{k_{m,l}}\left(\frac{\partial^2\theta}{\partial X^2}+\frac{\partial^2\theta}{\partial Y^2}\right)-\frac{\varepsilon}{Ste}\frac{\partial\phi(\theta)}{\partial\tau} \tag{12}$$

Energy balance for the conjugate solid wall (aluminium fins):

$$\frac{(\rho C_p)_w}{(\rho C_p)_{m,l}}\frac{\partial\theta_w}{\partial\tau}=\left(\frac{k_w}{k_{m,l}}\right)\left(\frac{\partial^2\theta_w}{\partial X^2}+\frac{\partial^2\theta_w}{\partial Y^2}\right) \tag{13}$$

The adiabatic condition at the insulated walls:

$$\frac{\partial\theta_w}{\partial N}=0 \tag{14a}$$

where N is the non-dimensional normal to the insulated walls. The convective heat transfer at the heatsink top:

$$\left(\frac{k_w}{k_{m,l}}\right)\frac{\partial\theta_w(x,\,l_h)}{\partial H}=Bi\theta_w \tag{14b}$$

with $Bi=h_\infty H/k_{m,l}$

The uniform heat flux at the heatsink bottom:

$$\left(\frac{k_w}{k_{m,l}}\right)\frac{\partial\theta_w(X,\,0)}{\partial Y}=\delta(\tau) \tag{14c}$$

where $\delta(\tau)=\begin{cases}1+\gamma & 0<\tau<\tau_1\\ 1 & \tau<0,\ \tau>\tau_1\end{cases}$ and $\tau_1=\frac{t_1\alpha_{m,l}}{H^2}$.

The non-dimensional boundary conditions at the wall-porous interface are:

$$\theta_w|_{wall}=\theta_l|_{porous}\ \ and\ \ \left.\frac{k_w}{k_{m,l}}\frac{\partial\theta_w}{\partial n}\right|_{wall}=\left.\frac{k_m}{k_{m,l}}\frac{\partial\theta_l}{\partial n}\right|_{porous} \tag{14d}$$

The non-dimensional initial condition is the steady-state temperature and velocity distribution when $\delta(\tau)=1$, such as:

$$\theta(X,\,Y,\,0)=\theta@\ \text{steady}-\text{state},\ U(X,\,Y,\,0)=U@\ \text{steady}-\text{state, and}\ V(X,\,Y,\,0)=V@\ \text{steady}-\text{state} \tag{14e}$$

The dimensionless thermophysical properties are also introduced as:

$$\frac{k_{m,s}}{k_{m,l}}=\frac{(1-\varepsilon)k_p+\varepsilon k_s}{(1-\varepsilon)k_p+\varepsilon k_l}\ \text{and}\ \frac{k_w}{k_{m,l}}=\frac{k_w}{(1-\varepsilon)k_p+\varepsilon k_l} \tag{15a}$$

$$\frac{(\rho C_p)_w}{(\rho C_p)_{m,l}}=\frac{(\rho C_p)_w}{(1-\varepsilon)(\rho C_p)_p+\varepsilon(\rho C_p)_l}\ \text{and}\ \frac{(\rho C_p)_{m,s}}{(\rho C_p)_{m,l}}=\frac{(1-\varepsilon)(\rho C_p)_p+\varepsilon(\rho C_p)_s}{(1-\varepsilon)(\rho C_p)_p+\varepsilon(\rho C_p)_l} \tag{15b}$$

Table. 2
The specifications of the computational meshes

Cases	Domain Elements	Boundary Elements
Case 1	1233	217
Case 2	1732	275
Case 3	2773	345
Case 4	7139	596
Case 5	9089	716
Case 6	11330	832

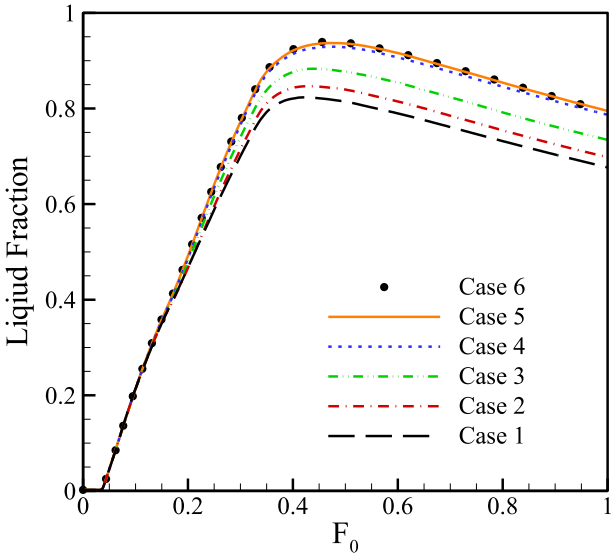

Fig. 2. The melt volume fraction (*MVF*) calculated using different mesh sizes

$$\phi(\theta)=\begin{cases}0 & \theta<\theta_f-\frac{\delta\theta}{2}\\ \frac{\theta-\theta_f}{\delta\theta} & \theta_f-\frac{\delta\theta}{2}<\theta<\theta_f+\frac{\delta\theta}{2}\\ 1 & \theta>\theta_f+\frac{\delta\theta}{2}\end{cases} \tag{16}$$

where $\delta\theta=\delta T/\Delta T$. The Darcy number and porosity are respectively equal to Da and$\varepsilon(X,\ Y)=\varepsilon_0$in the region filled with metal foam. Otherwise, Darcy→0 and $\varepsilon=1$ in the clear regions without metal foam. The non-dimensional temperature of the bottom wall is the parameter characterizing the heat transfer of the heatsink and is defined as:

$$\theta_b=\frac{T_b-T_\infty}{\Delta T}\ at\ Y=0 \tag{17}$$

θ_b represents the local wall temperature. The average temperature of the bottom wall can be correspondingly defined as:

$$\theta_{b,ave}=\frac{\int_0^{L_h}\theta_b}{L_h} \tag{18}$$

Finally, the volume fraction of melted PCM is calculated as:

$$MVF=\frac{\int_A\varepsilon\phi dA}{\int_A\varepsilon dA} \tag{19}$$

The enhancement due to the use of the PCM heatsink can be evaluated by comparing the average surface temperature of the hot element when the PCM heatsink is present to the case where the surface is directly cooled with the convection coefficient of h_∞. In the case of direct cooling of the hot element, the energy balance is $q''=h_\infty(T_{b,0}-T_\infty)$. The subscript 0 is adopted for the temperature of the element without the heatsink. Using the non-dimensional parameters, the energy balance can be written as $\theta_b=q''/(h_\infty\Delta T)$. Now, by invoking the definition of temperature scale and Biot number as $\Delta T=q''H/k_{m,l}$ and $Bi=h_\infty H/k_{m,l}$, the non-dimensional hot element temperature is re-written as

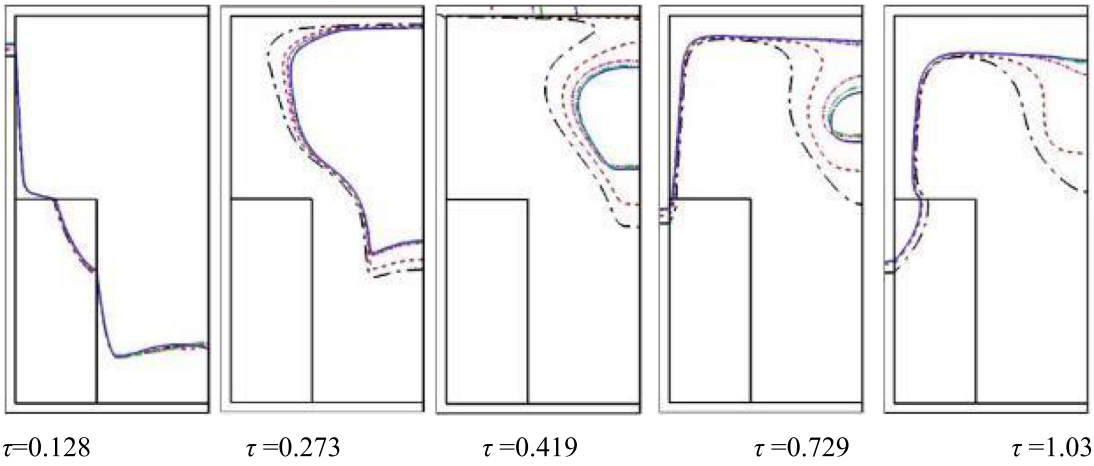

Fig. 3. The effect of mesh size on the phase change interface (*MVF =0.5*) at difference dimensionless time. (Case 1 (Black long dash-dot), Case 3 (Red Dashed), Case 4 (Pink dash-dot), Case 5 (Green dash-dot-dot), Case 6 (Blue solid)

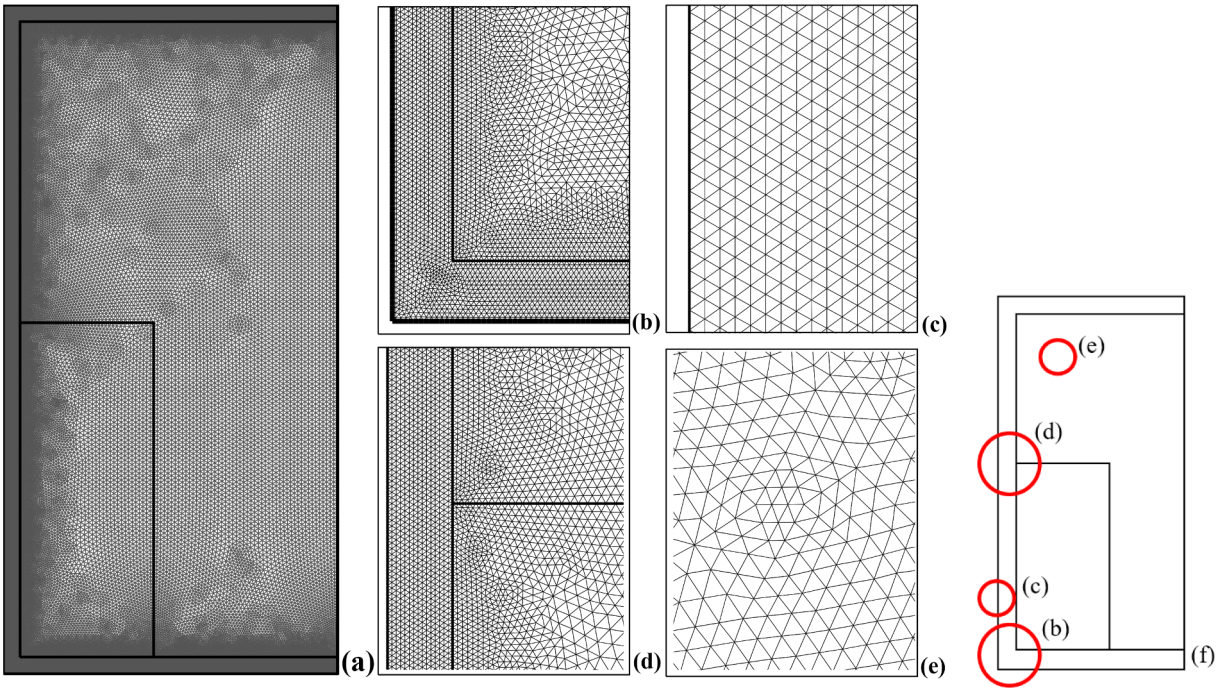

Fig. 4. A view of the initial mesh of Case 5

$\theta_{b,o} = 1/Bi$. It should be noted that as the surface heat flux of the element is uniform and the convective heat transfer coefficient is also uniform, the local surface temperature of the hot element is equal to the average temperature of the element. The level of heat transfer enhancement due to the presence of the PCM heatsink is evaluated using the parameter:

$$\eta_0 = \frac{\theta_{b,ave}}{\theta_{b,0}} \tag{20}$$

A value of η_0 higher than unity denote the enhancement of the heat transfer due to the heatsink while the values of η_0 lower than unity indicate reduction of heat transfer due to the presence of the heatsink.

3. Numerical method, grid check, and validation

3.1. Numerical method

Here, a Finite Element Method (FEM) is developed to solve the governing equations of (10)–(13) along with the corresponding boundary conditions of Eq. 14 (a)–(d) and the initial condition of Eq. 14 (e). Following the FEM, the governing equations are written in a weak form, and the following basis set $\{\gamma_k\}_{k=1}^{N}$ is adopted to expand the x and y –velocity equations as well as the pressure, and the temperature equations. Mesh adaptation was employed in the phase transition area to increase the accuracy of the results. The mesh adaptation also improved the stability and convergence rate. More details about the numerical code are reported in our previous study [42].

3.2. Non-dimensional parameters

In order to calculate the non-dimensional parameters, the following temperature and geometrical specifications were adopted: $l_w = 0.1$ m, $l_h = l_w$, $T_f = 52°C$, $T_\infty = 10°C$, $h_\infty = 100$ W/m^{2}K, $q''_h = 2500$ kW/m^2, $\kappa = 1.2 \times 10^{-7}$, $\varepsilon = 0.975$, $s_b = s_t = s_w = 0.025 \times l_w$, $l_{hp} = 0.3 \times l_w$, $l_{wp} = 0.2 \times l_w$, $\gamma = 5$, $t_0 = 200$ and $t_1 = 1771.5$ so $\Delta t = t_1 - t_0 = 1571$ s. The fusion range is adopted as 6.5°C and $A_{mush} = 5 \times 10^{+5}$. The

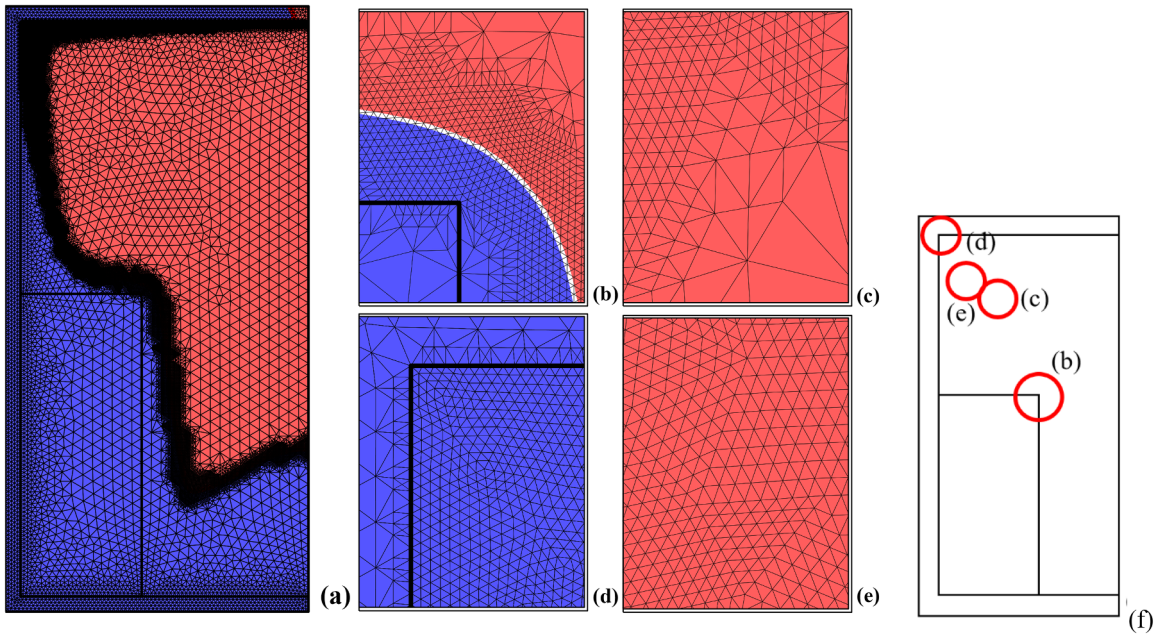

Fig. 5. A view of mesh Case 5 after adaptation when $\tau = 0.1823$.

remaining thermophysical properties for copper and paraffin-wax are adopted from Table 1. The initial temperature is adopted as $T = T_\infty$. Base on this case study, the non-dimensional parameters are evaluated as: $Da = 1.2 \times 10^{-5}$, $Bi = 2.606$, $Ra = 4.8709 \times 10^{+7}$, $Pr = 1.975$, $\theta_f = 0.644°C$, $\delta\theta = 0.1$. The other parameters are evaluated as $\Delta T = 65.17$, $\Delta\tau = 0.287$ so $\tau_0 = 0.03646$ and $\tau_1 = 0.323$. The non-dimensional geometrical variables are $S_b = S_t = S_w = 0.025$, $L_{hp} = 0.3$ and $L_{wp} = 0.2$. This set of the non-dimensional parameters is adopted for the presentation of the research outcomes. Otherwise, the value of the non-dimensional parameter will be stated.

3.3. Grid check

In order to check the overall quality of the utilized unstructured mesh in the domain of the solution, six different mesh sizes with total element numbers of 1450, 2007, 3118, 7735, 9805, and 12132 are used as cases 1-6, respectively. Specifications of the examined meshes are reported in Table 2. Fig. 2 depicts the melt volume fraction as a function of time computed by using various mesh sizes. As seen, the size of the mesh can notably affect the computations. However, for a mesh with total elements above 7735 (Case 4), the melting volume fraction is independent of the utilized mesh size. The phase change interface for various mesh sizes is plotted in Fig. 3. The phase change interface of Case 2 is not plotted here to avoid congestion. The phase change interfaces are plotted for various time steps, including start of melting ($\tau = 0.128$), sufficient time after start of melting ($\tau = 0.273$), after the highest liquid fraction reaches ($\tau = 0.419$), sometime after the pulse heat flux turns of ($\tau = 0.729$), long time after pulse heat turns off and solidification advances in the heatsink ($\tau = 1.03$). As seen, the meshes of Cases 4, 5, and 6 are almost coincident. Hence, for the sake of computational costs, the mesh of Case 5 is selected as the computational mesh of the current work.

Fig. 4 illustrates the utilized mesh of Case 5, which was selected for computations at an initial time with no adaptations. The magnified regions are indicated in Fig. 4(f). As seen, the initial mesh is denser next to walls to effectively capture the boundary layer temperature and velocity gradients. Fig. 5 displays the utilized mesh at a sufficiently large time, $\tau = 0.1823$. The selected regions were magnified according to the circles denoted Fig. 5 (f). Each of the selected regions shows an important feature of the utilized mesh. The red and blue regions are the liquid and solid regions, respectively. The mesh adaptation is evident at the phase change interface, *i.e.*, the interface of the liquid and solid regions). It is also clear that the adapted area around the phase change interfaces adequately encloses the interface.

3.4. Validations

The results of the present model and numerical code are compared with several numerical and experimental literature-works. As a comparison, a cavity filled with a porous medium is adopted. The top and bottom walls of the cavity are well insulated while the side walls are at hot and cold isothermal temperatures. Assuming a very high value of Darcy number (Darcy flow) and no phase change heat transfer, the average Nusselt number in the present study is obtained as 3.111, and it was reported as 3.113 [49] and 3.104 [50] for $Ra \times Da = 100$. The results of the present code are also compared with the studies of Zheng et al. [19] and the studies of [51–55] were the details are reported in our previous work [42].

4. Results and discussions

Fig. 6 illustrates the evolution of the streamlines of melted PCM and the temperature contours with time inside the cavity. Zones with no streamlines indicate that the PCM is in the solid-state, as no flow is occurring. Initially (Fig. 6 (a)), there is no flow in the cavity. Right after the activation of the heat pulse (Fig. 6 (b)), the PCM starts to melt near the cavity bottom. In the first stages of the heat pulse (Fig. 6 (c) to (f)), the melting intensifies in the porous foam region, while being less developed in the zone with no foam. A high temperature-gradient also appears in the solid region. These observations point out the effect of the porous foam on the enhancement of the PCM thermal conductivity. In fact, as the conductivity increases in the porous zone, the heat is transferred faster in the PCM, which melts consequently. During the heat pulse (Fig. 7 (g), (h) and (i)), the PCM follows the same trend. Melting occurs more significantly near and in the porous foam compared to the neighboring zone.

The melting front is close to the top wall in the porous foam, while it remains near the cavity center in the zone with no foam. In the last stage of the heat pulse (Fig. 6 (j)), the melting front reaches the top wall above the porous foam while it remains near the cavity center in the

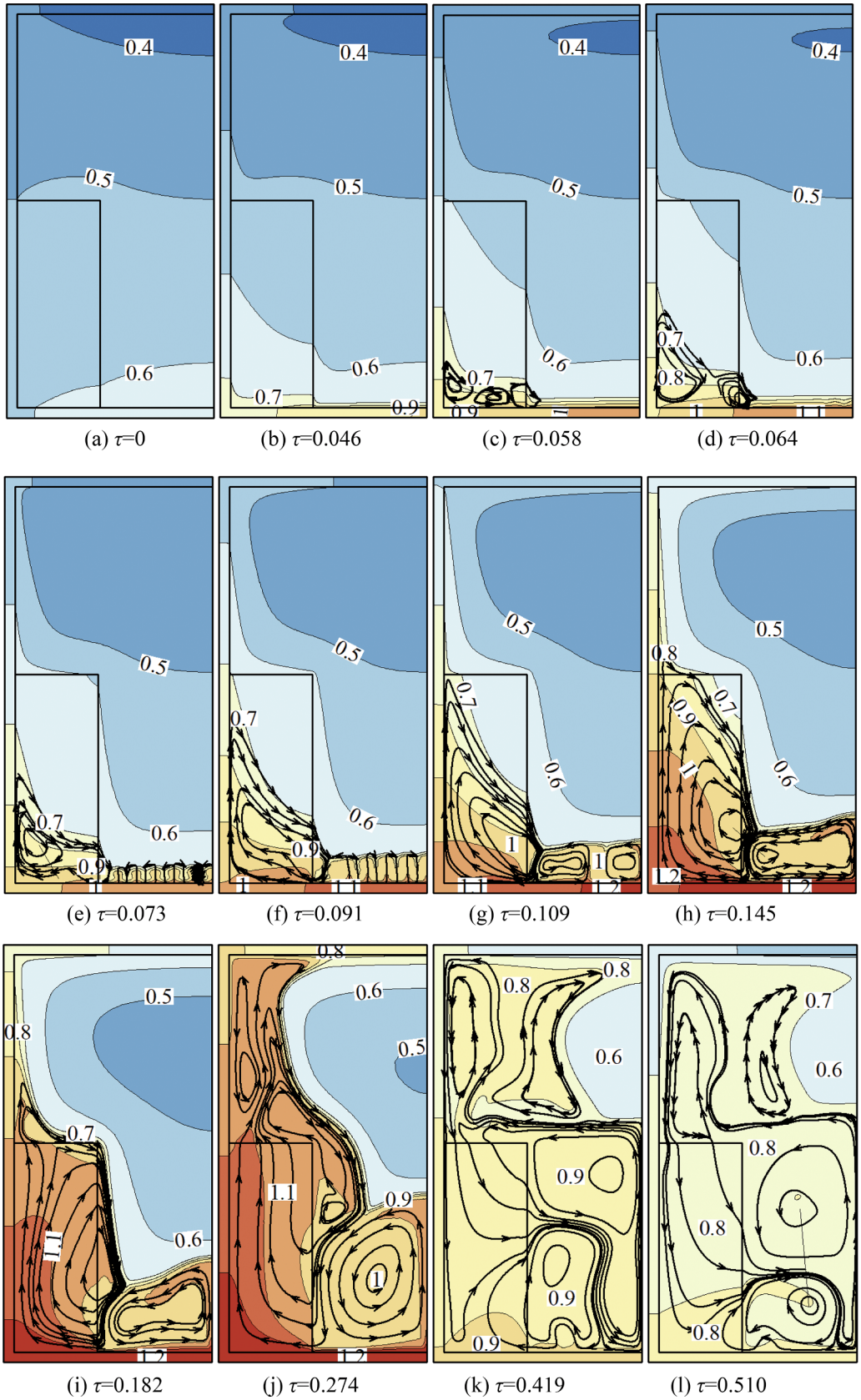

Fig. 6. The contours of the streamlines and isotherms at various time-snaps of phase change for $\theta_f = 0.6444$

other zones. Shortly after the heat pulse is turned off (Fig. 6 (k) and (l)), melting continues all over the cavity zone and only a small portion of the PCM remains in the solid-state near the top right corner of the cavity, despite the fact that power at the bottom wall is back to its steady value. As time goes (Fig. 6 (m), (n), and (o)), the PCM starts to solidify near the cavity top and above the porous foam. After a

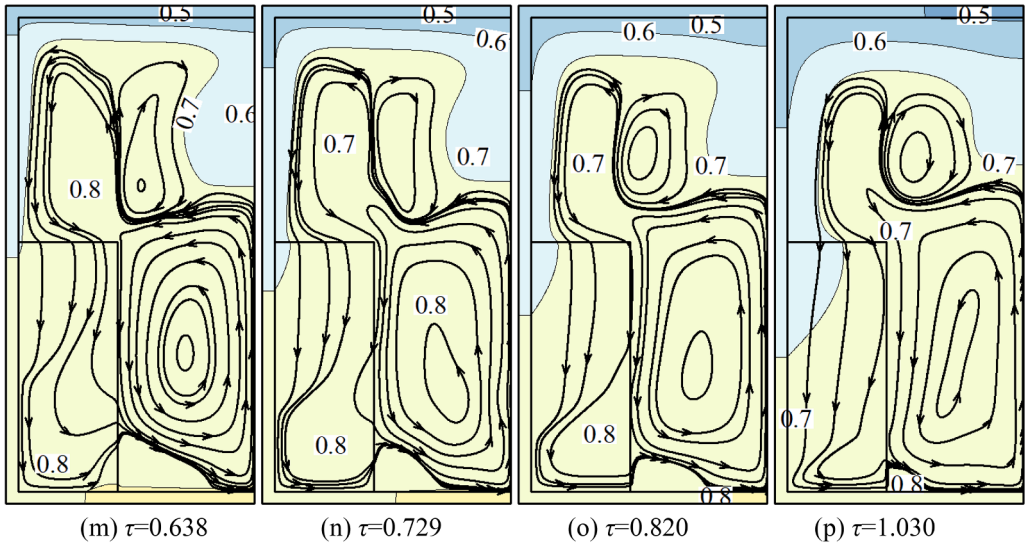

Fig. 6. (*continued*)

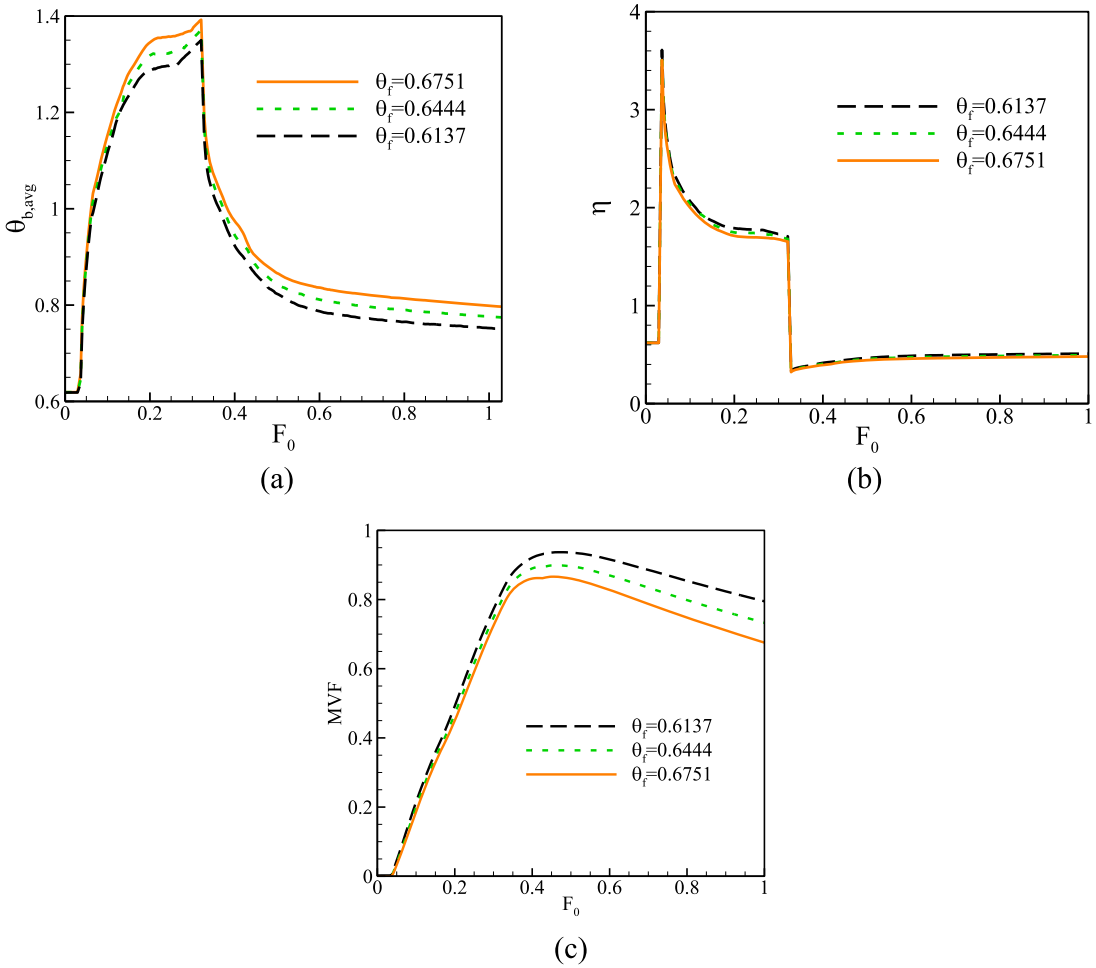

Fig. 7. Time history of the heatsink characteristics at various values of θ_f when $Bi = 2.6069$; (a): the dimensionless wall temperature ($\theta_{b,ave}$), (b): the heatsink efficiency (η), and (c): the melt volume fraction (*MVF*)

sufficiently long time, solid PCM is covering the top part of the cavity and a small part of the porous foam, while the major part of the cavity is filled with melted PCM. This suggests that while the porous foam enhances the PCM melting when the heat pulse is activated, it has little effect on the solidification process of the PCM when the heat of the bottom wall returns to the steady-state.

The variation of the bottom wall average temperature $\theta_{b,avg}$, the heat enhancement efficiency η, and the melting volume fraction MVF as functions of time for different values of the fusion temperature θ_f is plotted in Fig. 7. Attention to Fig. 7 (a) shows that $\theta_{b,avg}$ is initially

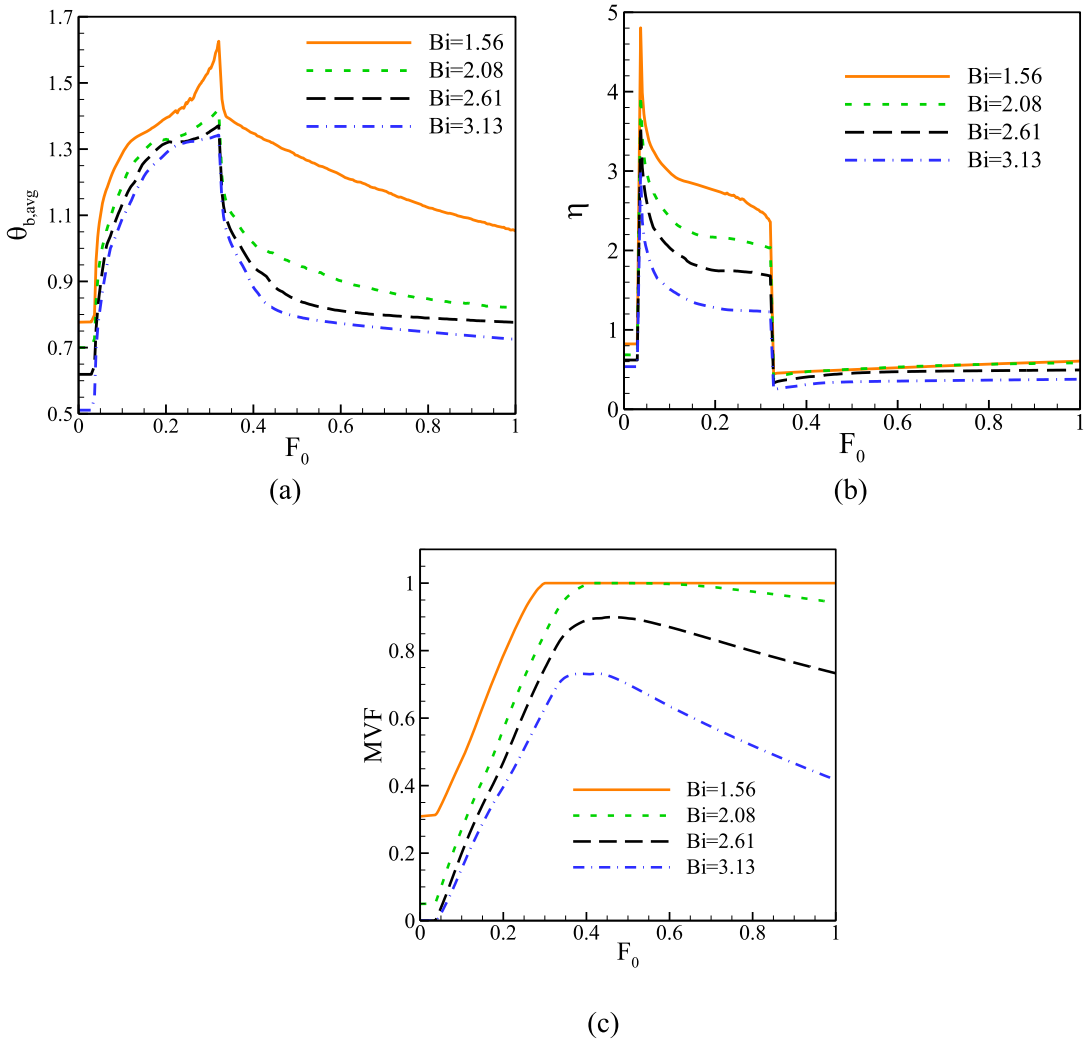

Fig. 8. Time history of the heatsink characteristics at various values of *Bi* when $\theta_f = 0.614$; (a): the dimensionless wall temperature ($\theta_{b,ave}$), (b): the heatsink efficiency (η), and (c): the melt volume fraction (*MVF*)

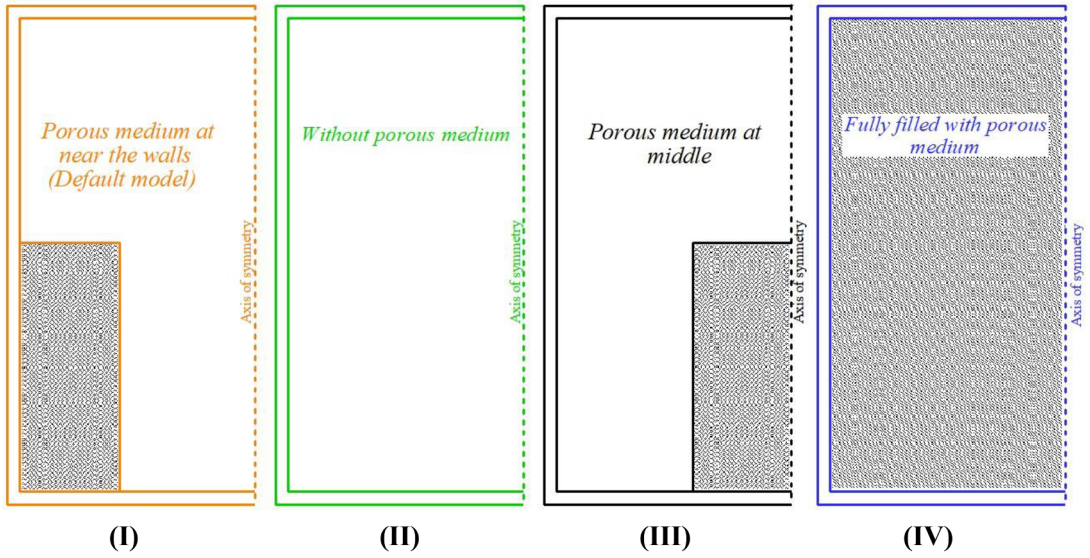

Fig. 9. Different locations of the metal foam layer in the heatsink

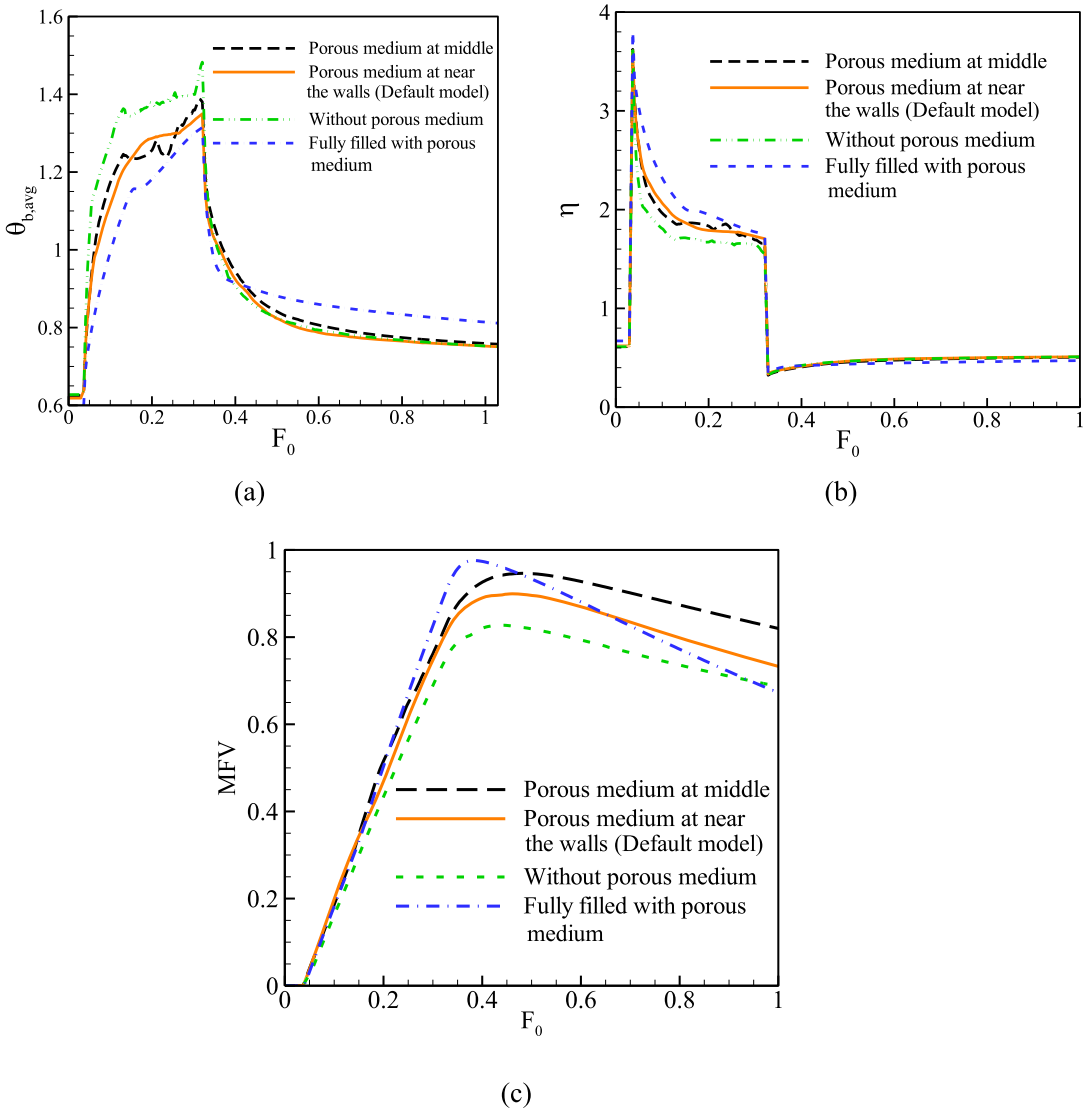

Fig. 10. Time history of the heatsink characteristics for different conditions of the porous medium when $\theta_f = 0.644$; (a): the dimensionless wall temperature ($\theta_{b,ave}$), (b): the heatsink efficiency (η), and (c): the melt volume fraction (*MVF*)

constant, then increases drastically when the heat pulse is activated and reaches its maximum value at the end of the pulse. Once the pulse is turned off, the temperature drops sharply for a short period then decreases slowly as time goes. Similarly, it is shown in Fig. 7 (b) that the efficiency increases significantly on the initiation of the heat pulse, then decreases and stabilizes above unity during the short period of the heat pulse, then decreases sharply at the end of the pulse and stabilizes at a value lower than unity. Indeed, the temperature difference between the hot wall and the melting interface is lower than that of the hot wall and the cooling external flow above the cavity. Thus, comparing the current model to the case where the hot wall is directly cooled by the external flow reveals that the thermal resistance of the PCM can be a barrier slowing down the cooling of the hot wall. However, the heat transfer due to convection with the PCM in the heatsink, as well as the PCM heat storage capability, is an extra factor improving the cooling of the hot wall. This can be seen in Fig. 7 (b). When the heat pulse is initiated, the sensible heat in the heatsink increases strongly the efficiency. Shortly after, the latent heat due to the melting of the PCM is also absorbed from the heat generated at the hot wall and further contributes to its cooling. When the power gets back to its steady low value, the external flow can more efficiently absorb the heat, and the presence of the heatsink is not advantageous.

Fig. 7 (a) and (b) show also that increasing the PCM fusion temperature θ_f increases the hot wall temperature $\theta_{b,avg}$ and slightly reduces the heatsink efficiency. This behavior can be understood by looking at Fig. 7 (c). This figure shows that when the heat pulse is initiated, the MVF increases indicating that the PCM is melting. The MVF starts dropping slowly at the end of the pulse and the PCM is undergoing solidification. Fig. 8 (c) additionally shows that increasing θ_f leads to a lower melting volume fraction MVF. The solid portion of the PCM is then greater for a higher θ_f. As no convection is occurring in the solid region, the thermal resistance in a heatsink with smaller molten PCM region increases, and, consequently, the heatsink efficiency is reduced.

Fig. 8 shows the effect of Biot number *Bi* on the variation of $\theta_{b,avg}$, η and MVF as a function of time. The shape of this variation is the same for all the values of *Bi* as explained in Fig. 7. Nonetheless, it is clear that while increasing *Bi* tends to reduce $\theta_{b,avg}$, it also reduces the heatsink efficiency η. Indeed, *Bi* is an indicator of the importance of the convective transfer with the external flow. Increasing *Bi* signifies that the external flow is absorbing more of the heat generated by the hot wall and decreasing its temperature $\theta_{b,avg}$. However, this decrease is not translated into a rise in the heatsink efficiency η. This is due to the fact that η is defined based on a comparison with a model where the hot

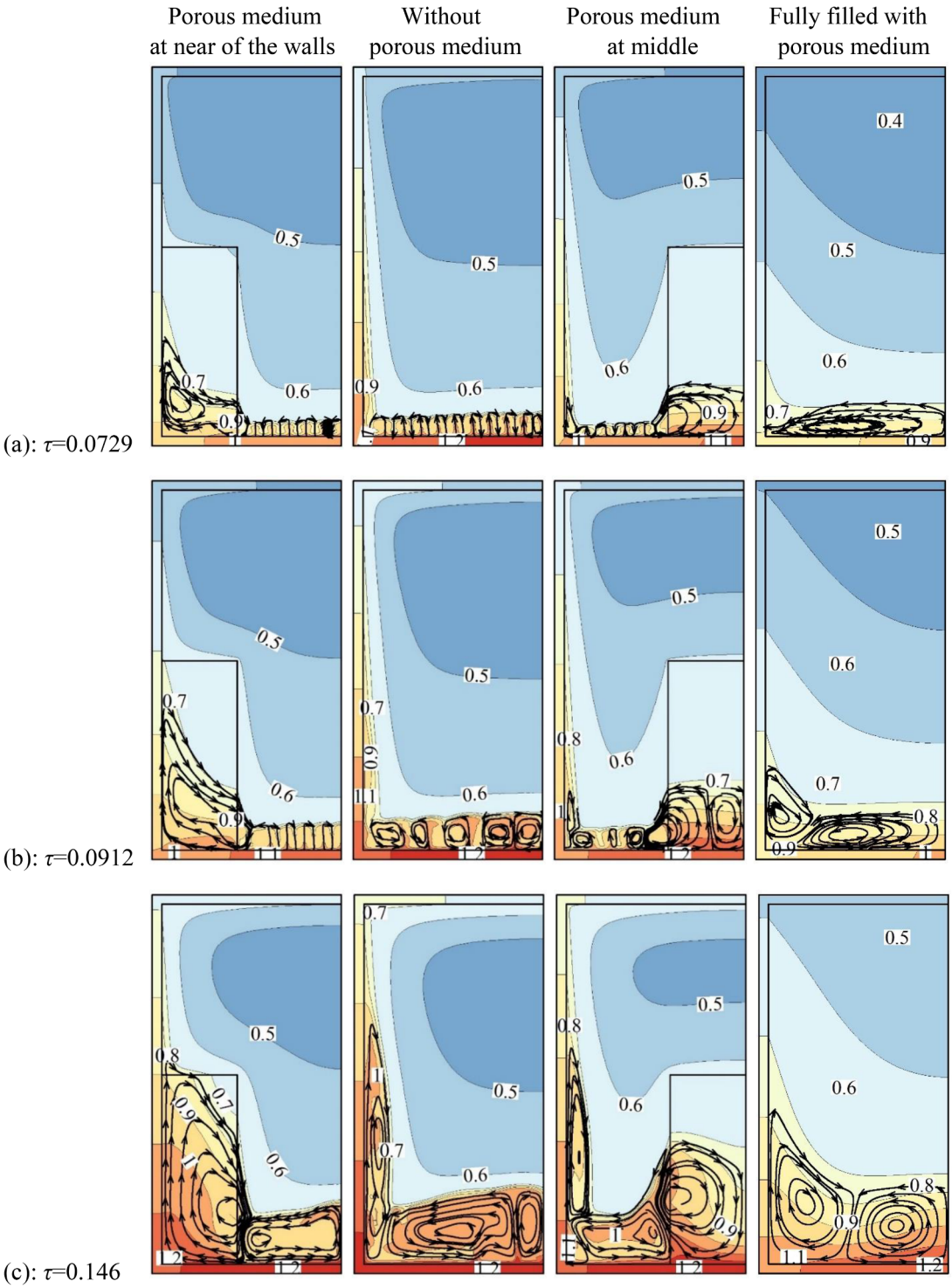

Fig. 11. The contours of the streamlines and isotherms at various time-snaps of phase change for different locations of the metal foam layer

wall is directly cooled by the external flow. Consequently, raising the contribution of the external flow to the cooling of the hot wall, by increasing *Bi*, reduces the heatsink efficiency. Another consequence is that, as the contribution of the PCM to the heat absorption is decreased, less melting is occurring, and the MVF is reduced throughout the cooling process, as can be seen in Fig. 8 (c).

In order to investigate the effect of the presence and the location of the porous foam on the heat transfer enhancement, three additional configurations are considered and compared to the default model. In total, four configurations are considered: (I) porous foam near the wall, (II) without porous foam, (III) porous foam in the middle, and (IV) a cavity fully filled with porous medium. These locations are depicted in Fig. 9.

The impact of the presence of the metal foam and the variation of its location on the variation of $\theta_{b,\,avg}$, η, and MVF as functions of time are shown in Fig. 10. The trend of this variation is the same in the four configurations. However, it is clear that the presence of the porous foam positively affects the heat transfer and enhances the cooling of the hot wall, mainly in the initial stages when conductive heat transfer is dominant. Figs. 10 (a) shows that the temperature of the hot wall is

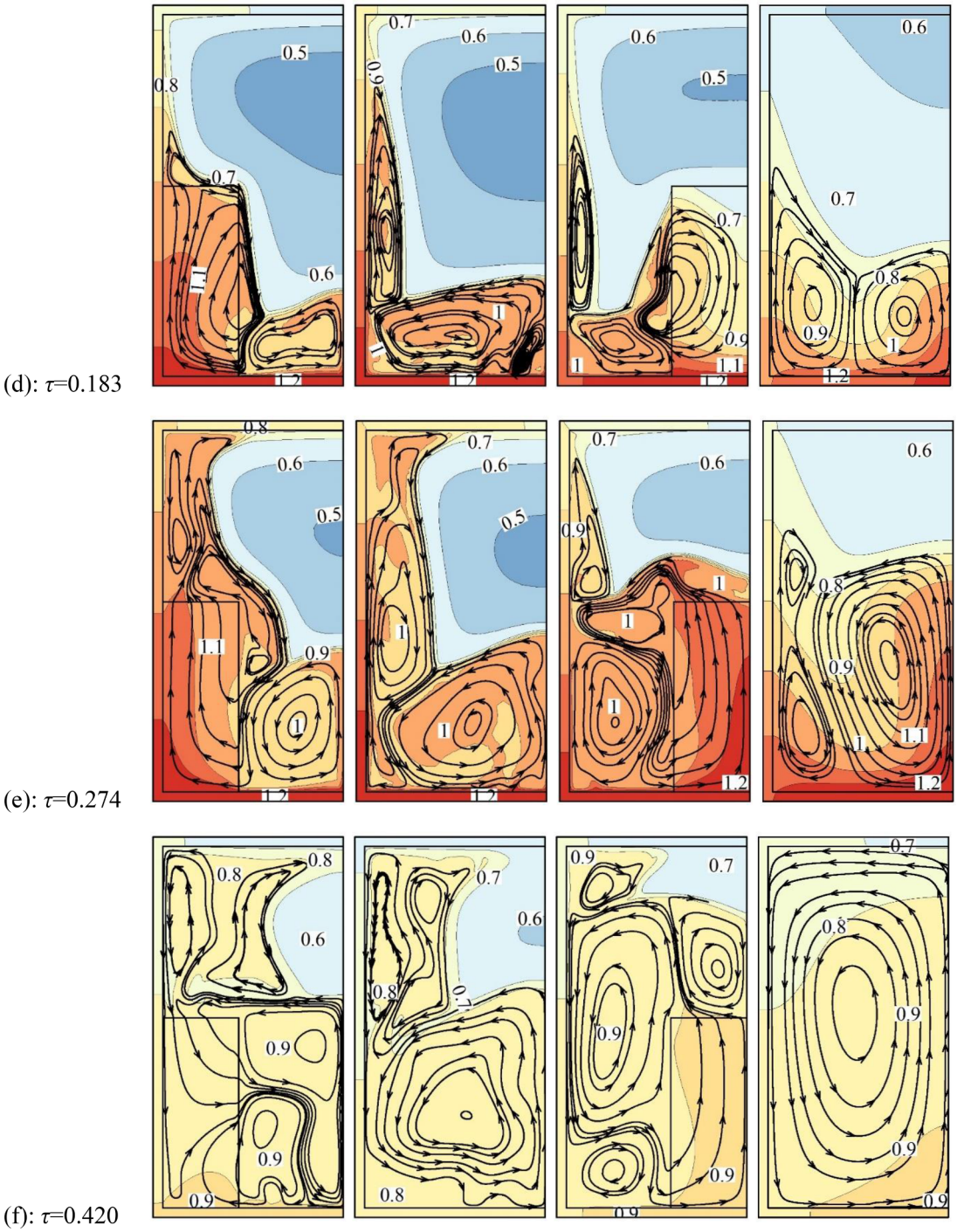

Fig. 11. (*continued*)

higher in the case without metal foam, and consequently, the efficiency is low as it can be seen in Fig. 10(b). This is since, at the early stages, the heat transfer is mainly conduction dominant, and the presence of the porous medium boosts the conduction heat transfer mechanism. After the initial stages, the portion of liquid PCM increases, and the natural convective heat transfer gets important. At this stage, the presence of a porous medium suppresses the flow circulation and reduces the heat transfer rate. Hence, it can be concluded that there should be an optimum amount of metal foam in the heatsink, which boosts the conduction heat transfer at the early stage but does not suppress the convection flow at the intermediate stages of heat transfer.

On the other hand, the location of the porous medium slightly affects the enhancement efficiency and shows a small fluctuation with time. Overall, the presence of the foam near the wall or in the middle leads roughly to the same heat transfer enhancement. Moreover, Fig. 10 (c) shows that the MVF is at its highest in the initial stages in a cavity fully filled with a metal foam. For the other configurations, the MVF is maximum when the porous medium is in the middle and is minimal in the absence of the porous foam. Using the configuration (I) tends then to reduce the MVF compared to the configuration (III) while leading almost to the same efficiency.

To better understand the effect of the porous foam location on the heat transfer characteristics, the streamlines and the temperature contours inside the cavity are plotted at different instants in Fig. 11 for the four configurations (I), (II), (III) and (IV). It is clear that, at any instant τ, the streamlines are more developed near and in the porous foam in

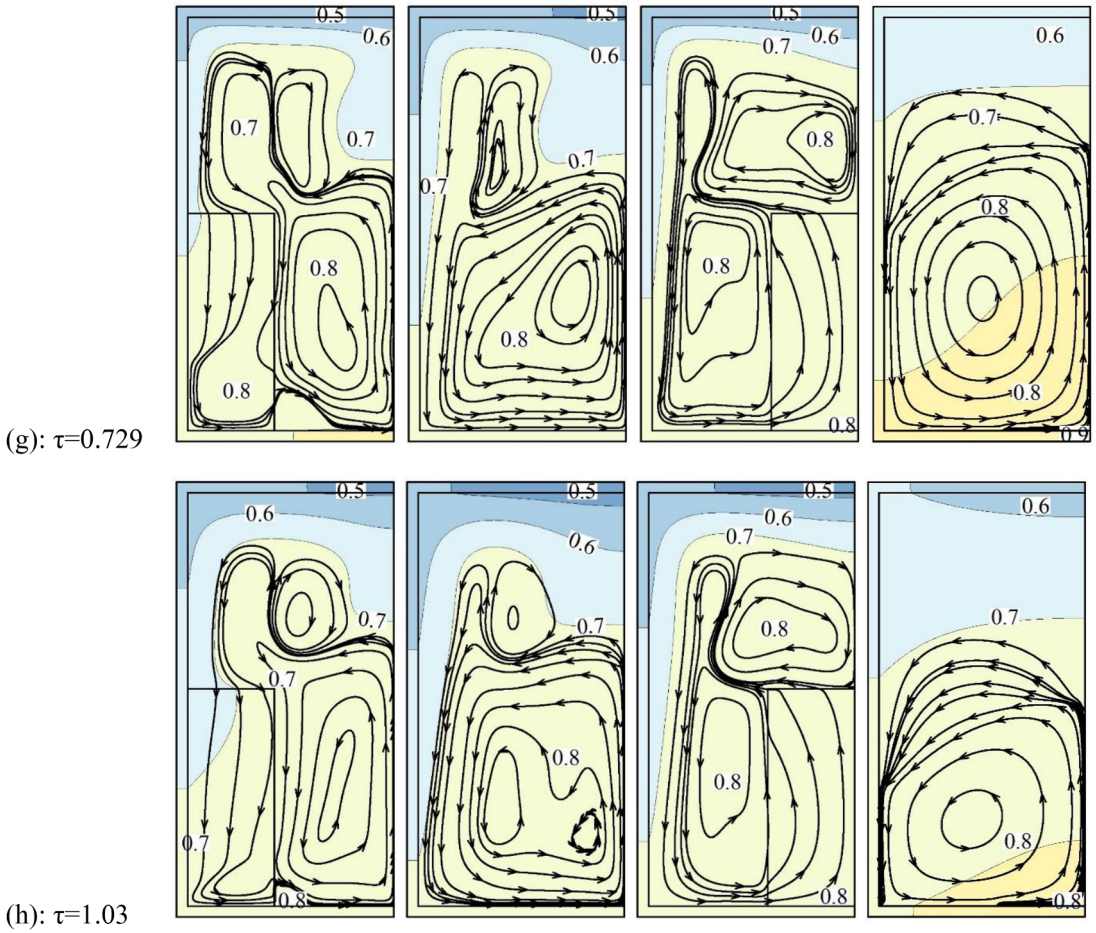

Fig. 11. (*continued*)

(I), (III) and (IV) compared to (II), indicating that the PCM melting is enhanced by the presence of the porous medium. In Fig. 11 (a) and (b), at the beginning of the heat pulse, the streamlines are more developed in the porous foam compared to the rest of the cavity in the configurations (I) and (III), while in configuration (II) are evenly developed in the bottom. In configuration (IV), a strong recirculation is concentrated near the bottom. Fig. 11 (c) and (d) show that in the first stage of the heat pulse, in the configurations (II) and (III), the melting of the PCM occurs at the bottom and in the thin layer adjacent to the insulated wall. In the last stage of the heat pulse (Fig. 11 (e)), the PCM is melting in the left part of the cavity and above the porous foam in configurations (I) and (III), while the amount of solid PCM is greater in configuration (II) compared to the other three. After the heat pulse is turned off (Fig. 11 (f)), the PCM keeps melting in all the configurations and covers the whole cavity in configuration (IV), almost the whole cavity in (I) and (III) except a small zone near the top right corner, while the solid PCM is always more expanded in (II).

After a long time (Fig. 11 (g) and (h)), the PCM starts to solidify from the top downwards and near the insulated wall in the first three configurations, while the solidification is occurring faster in configuration (IV) where the cavity is fully filled with porous medium. Moreover, in configuration (III), the solidification at the top is less evident than the other two configurations as more streamlines are developed in that zone. These results suggest that the symmetry of the model around the porous foam as well as its proximity to the insulated wall, as emphasized respectively in configurations (I) and (III), affect the distribution of the streamlines of the melted PCM inside the cavity and the location at which both melting solidification start and propagate. This can explain the small discrepancy between the two configurations in the efficiency and the MVF, as discussed in Fig. 10.

5. Conclusion

The natural convection flow and heat transfer in a PCM heatsink in the presence of a layer of metal foam is theoretically investigated. The governing equations are solved in the non-dimensional form using the finite element method. A grid adaptation method, controlled by the melt volume fraction, is utilized to increase the convergence and the resolution of the phase change heat transfer at the fusion interface. A BDF approach is also employed to adjust the solver time-steps automatically. The modeling approach and the numerical code are validated against experimental and numerical works available in the literature and found in good agreement. The effect of the fusion temperature of the PCM and the external cooling power on the isotherms and streamlines as well as the phase change interface and heatsink efficiency, was addressed. The main outcomes of the present study can be summarized as follows:

1- The heatsink improves the cooling during the active pulse when the heating power of the hot wall is high, but it is less advantageous when the power gets back to the steady power with a lower value.
2- Increasing the fusion temperature of the PCM raises the average temperature of the hot wall and reduces the efficiency of the heatsink. This is due to the fact that increasing the fusion temperature grows the solid region of the PCM in the cavity. As no convective heat transfer occurs in the solid PCM, the thermal resistance in the heatsink rises and leads to a reduction in the heatsink efficiency.
3- Increasing Biot number *Bi* reduces the average temperature of the hot wall and the efficiency of the heatsink, as well as the volume fraction of melted PCM. This is due to the increased contribution of the convective heat transfer with the external cooling flow. Biot

number represents the importance of the heat transfer by convection with the external flow. When *Bi* increases, more heat is absorbed by the external cooling flow, decreasing thus the average temperature of the hot wall. As the efficiency was defined by comparing the case with the heatsink to the case where the external flow is directly cooling the hot wall, the efficiency is reduced with the rise of *Bi* due to the increased contribution of the external flow to the hot wall cooling.

4- The porous metal foam enhances the melting of PCM melting when the heat pulse is activated by increasing the PCM thermal conductivity. The presence of the porous foam raises the efficiency of the heatsink and the melted volume fraction and reduces the temperature of the bottom wall.
5- The location of the porous foam inside the cavity affects the streamlines of the melted PCM and the locations of the melting and solidification zones in the cavity, but it has a negligible effect on the efficiency of the heatsink. Besides, the melt volume fraction increases when placing the porous foam in the middle of the cavity instead of near the wall.
6- A cavity fully filled with metal foam shows a lower temperature at the initial times where the portion of liquid PCM is small, and the heat transfer is conduction dominant. However, at the intermediate steps, the convection flows are strong due to the development of the liquid region. In this case, the metal foam (in a fully filled cavity) suppresses the natural convection flow and results in higher surface temperature and lower cooling efficiency.

In the present study, the weight and the shape of the porous layers were assumed to be constant, and only the effect of the location of the porous layer was investigated. The outcomes indicated that the presence of the layer of the porous medium could enhance the heatsink efficiency, but the effect of the location of the porous layer on the temperature of the hot element was negligible. On the other hand, a cavity fully filled with a metal foam shows poor heat transfer performance at intermediate stages. Hence, the optimization of the weight of the porous layer, including size, shape, and the porosity of the layer, can be pursued in future works.

CRediT authorship contribution statement

Ahmad Hajjar: Conceptualization, Methodology, Writing - review & editing, Investigation, Validation. **Esmail Jamesahar:** Formal analysis, Data curation, Validation. **Hassan Shirivand:** Formal analysis, Data curation, Validation. **Mohammad Ghalambaz:** Methodology, Writing - original draft, Supervision, Writing - review & editing. **Roohollah Babaei Mahani:** Methodology, Writing - original draft, Writing - review & editing, Supervision.

Declaration of Competing Interest

The authors clarify that there is no conflict of interest for report.

Supplementary materials

Supplementary material associated with this article can be found, in the online version, at doi:10.1016/j.est.2020.101701.

References

[1] Z. Khan, Z. Khan, A. Ghafoor, A review of performance enhancement of PCM based latent heat storage system within the context of materials, thermal stability and compatibility, Energy Convers. Manage. 115 (2016) 132–158.
[2] I. Sarbu, C. Sebarchievici, A comprehensive review of thermal energy storage, Sustainability 10 (1) (2018) 191.
[3] A. Crespo, et al., Latent thermal energy storage for solar process heat applications at medium-high temperatures–A review, Sol. Energy (2018).
[4] M.H. Abokersh, et al., Review of the phase change material (PCM) usage for solar domestic water heating systems (SDWHS), Int. J. Energy Res. 42 (2) (2018) 329–357.
[5] P.T. Sardari, et al., Discharge of a composite metal foam/phase change material to air heat exchanger for a domestic thermal storage unit, Renew. Energy 148 (2020) 987–1001.
[6] S. Chandel, T. Agarwal, Review of cooling techniques using phase change materials for enhancing efficiency of photovoltaic power systems, Renew. Sustain.Energy Rev. 73 (2017) 1342–1351.
[7] J. Jaguemont, et al., Phase-change materials (PCM) for automotive applications: A review, Appl. Therm. Eng. 132 (2018) 308–320.
[8] H. Bazai, et al., Numerical study of circular-elliptical double-pipe thermal energy storage systems, J. Energy Storage 30 (2020) 101440.
[9] A. Shahsavar, et al., Performance evaluation of melting/solidification mechanism in a variable wave-length wavy channel double-tube latent heat storage system, J. Energy Storage 27 (2020) 101063.
[10] S.K. Sahoo, M.K. Das, P. Rath, Application of TCE-PCM based heat sinks for cooling of electronic components: a review, Renew. Sustain. Energy Rev. 59 (2016) 550–582.
[11] Z. Li, et al., Effect of porous medium and nanoparticles presences in a counter-current triple-tube composite porous/nano-PCM system, Appl. Therm. Eng. 167 (2020) 114777.
[12] N.S. Bondareva, et al., Heat transfer performance of the finned nano-enhanced phase change material system under the inclination influence, Int. J. Heat Mass Transfer 135 (2019) 1063–1072.
[13] C.-J. Ho, et al., Cooling performance of MEPCM suspensions for heat dissipation intensification in a minichannel heat sink, Int. J. Heat Mass Transfer 115 (2017) 43–49.
[14] M. Eisapour, et al., Exergy and energy analysis of wavy tubes photovoltaic-thermal systems using microencapsulated PCM nano-slurry coolant fluid, Appl. Energy 266 (2020) 114849.
[15] A. Shahsavar, et al., Thermal performance evaluation of non-uniform fin array in a finned double-pipe latent heat storage system, Energy 193 (2020) 116800.
[16] P.T. Sardari, et al., Energy recovery from domestic radiators using a compact composite metal Foam/PCM latent heat storage, J. Cleaner Prod. 257 (2020) 120504.
[17] Talebizadeh Sardari, et al., Numerical modelling of phase change material melting process embedded in porous media: effect of heat storage size. Proceedings of the institution of mechanical engineers, Part A: J. Power Energy 234 (3) (2020) 365–383.
[18] X. Xiao, P. Zhang, M. Li, Preparation and thermal characterization of paraffin/metal foam composite phase change material, Appl. Energy 112 (2013) 1357–1366.
[19] H. Zheng, et al., Thermal performance of copper foam/paraffin composite phase change material, Energy Convers. Manage. 157 (2018) 372–381.
[20] A. Dinker, M. Agarwal, G. Agarwal, Heat storage materials, geometry and applications: A review, J. Energy Inst. 90 (1) (2017) 1–11.
[21] A. Mallow, O. Abdelaziz, S. Graham, Thermal charging performance of enhanced phase change material composites for thermal battery design, Int. J. Therm. Sci. 127 (2018) 19–28.
[22] A. Mallow, et al., Investigation of the stability of paraffin–exfoliated graphite nanoplatelet composites for latent heat thermal storage systems, J. Mater. Chem. 22 (46) (2012) 24469–24476.
[23] M.S. Astanina, M. Sheremet, C.J. Umavathi, Unsteady natural convection in a partially porous cavity having a heat-generating source using local thermal non-equilibrium model, Int. J. Numer. Methods Heat Fluid Flow (2019).
[24] N. Gibanov, M.A. Sheremet, Effect of trapezoidal heater on natural convection heat transfer and fluid flow inside a cubical cavity, Int. J. Numer. Methods Heat Fluid Flow (2019).
[25] A. Alsabery, et al., Effects of two-phase nanofluid model on MHD mixed convection in a lid-driven cavity in the presence of conductive inner block and corner heater, J. Therm. Anal. Calorim. 135 (1) (2019) 729–750.
[26] A. Alsabery, et al., Conjugate natural convection of Al2O3–water nanofluid in a square cavity with a concentric solid insert using Buongiorno's two-phase model, Int. J. Mech. Sci. 136 (2018) 200–219.
[27] I. Hashim, et al., Numerical investigation of natural convection of Al2O3-water nanofluid in a wavy cavity with conductive inner block using Buongiorno's two-phase model, Adv. Powder Technol. 30 (2) (2019) 399–414.
[28] A.I. Alsabery, et al., Effects of two-phase nanofluid model and localized heat source/sink on natural convection in a square cavity with a solid circular cylinder, Comput. Meth. Appl. Mech. Eng. 346 (2019) 952–981.
[29] A. Alsabery, et al., MHD convective heat transfer in a discretely heated square cavity with conductive inner block using two-phase nanofluid model, Sci. Rep. 8 (1) (2018) 7410.
[30] A. Rashad, et al., Magnetohydrodynamics natural convection in a triangular cavity filled with a Cu-Al2O3/water hybrid nanofluid with localized heating from below and internal heat generation, J. Heat Transfer 140 (7) (2018) 072502.
[31] A. Alsabery, et al., Numerical investigation of mixed convection and entropy generation in a wavy-walled cavity filled with nanofluid and involving a rotating cylinder, Entropy 20 (9) (2018) 664.
[32] N.S. Bondareva, et al., Heat transfer inside cooling system based on phase change material with alumina nanoparticles, Appl. Therm. Eng. 144 (2018) 972–981.
[33] N. Bondareva, M. Sheremet, Numerical investigation of the two-dimensional natural convection inside the system based on phase change material with a source of volumetric heat generation, Thermophys. Aeromech. 25 (4) (2018) 525–537.
[34] N.S. Bondareva, M.A. Sheremet, Numerical simulation of melting of phase change material in a square cavity with a heat source, Key Engineering Materials, Trans Tech Publ, 2016.

[35] M. Ghalambaz, T. Groşan, I. Pop, Mixed convection boundary layer flow and heat transfer over a vertical plate embedded in a porous medium filled with a suspension of nano-encapsulated phase change materials, J. Mol. Liq. 293 (2019) 111432.
[36] M. Ghalambaz, A.J. Chamkha, D. Wen, Natural convective flow and heat transfer of Nano-Encapsulated Phase Change Materials (NEPCMs) in a cavity, Int. J. Heat Mass Transfer 138 (2019) 738–749.
[37] B.V.S. Dinesh, A. Bhattacharya, Effect of foam geometry on heat absorption characteristics of PCM-metal foam composite thermal energy storage systems, Int. J. Heat Mass Transfer 134 (2019) 866–883.
[38] R. Hossain, et al., Energy storage system based on nanoparticle-enhanced phase change material inside porous medium, Int. J. Therm. Sci. 91 (2015) 49–58.
[39] A. Hussain, C. Tso, C.Y. Chao, Experimental investigation of a passive thermal management system for high-powered lithium ion batteries using nickel foam-paraffin composite, Energy 115 (2016) 209–218.
[40] W. Wu, et al., An experimental study of thermal management system using copper mesh-enhanced composite phase change materials for power battery pack, Energy 113 (2016) 909–916.
[41] Z.-Q. Zhu, et al., Transient performance of a PCM-based heat sink with a partially filled metal foam: effects of the filling height ratio, Appl. Therm. Eng. 128 (2018) 966–972.
[42] M. Ghalambaz, J. Zhang, Conjugate solid-liquid phase change heat transfer in heatsink filled with phase change material-metal foam, Int. J. Heat Mass Transfer 146 (2020) 118832.
[43] D.A. Nield, A. Bejan, Convection in porous media, Springer Science & Business Media, 2006.
[44] J. Buongiorno, Convective transport in nanofluids, J. Heat Transfer 128 (3) (2006) 240–250.
[45] M. Sheikholeslami, M. Shamlooei, R. Moradi, Fe3O4-Ethylene glycol nanofluid forced convection inside a porous enclosure in existence of Coulomb force, J. Mol. Liq. 249 (2018) 429–437.
[46] A. Bhattacharya, V.V. Calmidi, R.L. Mahajan, Thermophysical properties of high porosity metal foams, Int. J. Heat Mass Transfer 45 (5) (2002) 1017–1031.
[47] L. Betchen, A.G. Straatman, B.E. Thompson, A nonequilibrium finite-volume model for conjugate fluid/porous/solid domains, Numer. Heat Transf., Part A: Appl. 49 (6) (2006) 543–565.
[48] N.H. Saeid, Conjugate natural convection in a porous enclosure sandwiched by finite walls under thermal nonequilibrium conditions, J. Porous Media 11 (3) (2008).
[49] C. Beckermann, R. Viskanta, S. Ramadhyani, A numerical study of non-Darcian natural convection in a vertical enclosure filled with a porous medium, Numer. Heat Transf. 10 (6) (1986) 557–570.
[50] M.A. Sheremet, I. Pop, Natural convection in a square porous cavity with sinusoidal temperature distributions on both side walls filled with a nanofluid: Buongiorno's mathematical model, Transp. Porous Media 105 (2) (2014) 411–429.
[51] C. Gau, R. Viskanta, Melting and solidification of a pure metal on a vertical wall, J. Heat Transfer 108 (1) (1986) 174–181.
[52] J. Khodadadi, S. Hosseinizadeh, Nanoparticle-enhanced phase change materials (NEPCM) with great potential for improved thermal energy storage, Int. Commun. Heat Mass Transfer 34 (5) (2007) 534–543.
[53] S. Kashani, et al., Solidification of nano-enhanced phase change material (NEPCM) in a wavy cavity, Heat Mass Transf. 48 (7) (2012) 1155–1166.
[54] S. Tiari, S. Qiu, M. Mahdavi, Numerical study of finned heat pipe-assisted latent heat thermal energy storage system, in APS Meet. Abstr. (2014).
[55] A. Brent, V.R. Voller, K. Reid, Enthalpy-porosity technique for modeling convection-diffusion phase change: application to the melting of a pure metal, Numer. Heat Transf., Part A Appl. 13 (3) (1988) 297–318.